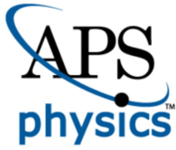

CHORUS

This is the accepted manuscript made available via CHORUS. The article has been published as:

Mapping Thermal Expansion Coefficients in Freestanding 2D Materials at the Nanometer Scale

Xuan Hu, Poya Yasaei, Jacob Jokisaari, Serdar Öğüt, Amin Salehi-Khojin, and Robert F. Klie

Phys. Rev. Lett. **120**, 055902 — Published 2 February 2018

DOI: 10.1103/PhysRevLett.120.055902

Mapping Thermal Expansion Coefficients in Free-Standing 2D Materials at the Nanometer Scale

Xuan Hu,[1] Poya Yasaei,[2] Jacob Jokisaari,[1] Serdar Öğüt,[1] Amin Salehi-Khojin,[2] and Robert F. Klie[1]

[1]*Department of Physics, University of Illinois at Chicago, Chicago, IL 60607, USA*

[2]*Department of Mechanical and Industrial Engineering, University of Illinois at Chicago, Chicago, IL 60607, USA*

(Dated: December 21, 2017)

Abstract

Two-dimensional materials, including graphene, transition metal dichalcogenides (TMDs) and their heterostructures, exhibit great potential for a variety of applications, such as transistors, spintronics, and photovoltaics. While the miniaturization offers remarkable improvements in electrical performance, heat dissipation and thermal mismatch can be a problem in designing electronic devices based on two-dimensional materials. Quantifying the thermal expansion coefficient of 2D materials requires temperature measurements at nanometer scale. Here, we introduce a novel nanometer-scale thermometry approach to measure temperature and quantify the thermal expansion coefficients in 2D materials based on scanning transmission electron microscopy combined with electron energy-loss spectroscopy to determine the energy-shift of the plasmon resonance peak of 2D materials as a function of sample temperature. By combining these measurements with first-principles modelling, the thermal expansion coefficients (TECs) of single-layer and free-standing graphene and bulk, as well as monolayer MoS_2, $MoSe_2$, WS_2, or WSe_2 are directly determined and mapped.

The combination of graphene, which has a zero bandgap, with semiconducting two-dimensional (2D) transition metal dichalcogenides (TMDs) has the potential to revolutionize the field of high power/high frequency electronics, leading to novel nanometer-scale devices [1–9]. However, thermal management in such devices will be crucial, due to the reduced dimensionality and high density of the devices in tightly packed structures [10–14]. It was previously suggested that the presence of grain boundaries and heterointerfaces has a significant impact on the overall thermal transport properties of devices based on 2D materials [15]. Therefore, a better understanding of the limits set by heat dissipation through grain boundaries and interfaces must be developed. One fundamental obstacle to be overcome is the lack of spatial resolution in common temperature measurements.

To date, nanoscale thermometry is carried out either through scanning probe microscopy-based (SPM-based) techniques like scanning thermal microscopy [16–20] or non-contact optical methods, such as Raman, fluorescence, and luminescence thermometry [21–23]. In SPM-based methods, the temperature is measured via a calibrated sensor fabricated on the tip of an AFM cantilever, such as a thermistor, where the electrical resistance is proportional to the temperature when the probe is in contact and in thermal equilibrium with the system. Although a spatial resolution of a few nanometers has been reported by performing the measurements in high vacuum [20], the resolution of these methods is limited by the size of the cantilever tip and the tip-surface contact characteristics. On the other hand, the non-contact optical techniques, such as Raman, fluorescence, and luminescence thermometry utilize an indirect temperature-dependent phenomenon, then convert the measured signal into a temperature value. These techniques can provide an accurate temperature reading after a precise calibration, but the spatial resolution is limited by the optical diffraction limit. In both methods, particularly SPM, it is difficult to prepare free-standing specimens, and the measured material is often supported by a substrate. The effects of the substrate can be difficult to extract and will always impact the measurement.

In this work, we utilize non-contact thermometry beyond the optical diffraction limit using a combination of scanning transmission electron microscopy (STEM) and electron energy-loss spectroscopy (EELS) and first-principles modeling to map the local temperature and thermal expansion coefficient of 2D materials. More specifically, we develop an approach, based on the temperature-dependent plasmon energy shift, which is related to the thermal lattice expansion [24–27]. In 2D materials, such as graphene or TMDs, quantum confinement

and surface plasmon effects dominate the energy shift of the plasmon peaks [28–30], providing a novel and universal approach for measuring the temperature and determining the thermal expansion coefficient of atomically thin structures, including metallic [31] and semiconductor materials.

Free-standing graphene, MoS_2, $MoSe_2$, WS_2, and WSe_2 were prepared for transmission electron microscopy analysis using liquid phase exfoliation and drop casting on a holey-carbon film coated Cu mesh. Low-loss EEL spectra were collected for each material at 8 different sample temperatures, between T=373 K and 723 K in 50 K increments using a Gatan in-situ heating holder. All spectra were calibrated using the zero-loss peak, and the low-loss intensity was normalized with respect to a 40-60 eV energy-loss window, so that the normalization is not affected by the plasmon peak. The shift in plasmon energy as a function of the temperature was then measured for each material, thus providing a direct means of calibrating the temperature for each of the different materials and allowing the temperature to be mapped. The low-loss EEL spectra from a single monolayer of WSe_2 is shown in Figure 1A for several temperatures. Since the plasmon peaks are relatively broad, we fit two Lorentzian functions to the individual plasmon peak to improve the accuracy of determining the plasmon peak energy-shift (See Supplemental Material [32] for more details). For WSe_2, the energy shift is dE/dT=-2.7 meV/K: a shift towards lower energy occurs as the temperature increases from 373 K to 723 K. This shift follows an approximately linear relationship between the plasmon energy and temperature (Figure 1B). Similar measurements are carried out for the materials.

The effects of layer thickness were also considered ranging from monolayers to a few layers thick. The thickness, more specifically the number of layers, was found to also influence the plasmon peak shift, and this effect needs to be accounted for in order to extract the temperature signal. To measure the thickness of the nanoflakes in units of number of layers, the ratio of the inelastically scattered over the transmitted electrons was determined using the low-loss EELS log-ratio method (see Supplemental Material [32]). The rate of plasmon energy change as a function of temperature (dE/dT) for free standing graphene and TMDs as a function of thickness is presented in Figures 1C-E. Results indicate that graphene exhibits positive energy shift compared to TMDs. Moreover, in TMDs containing Se, the plasmon energy shifts appear to be higher for all thicknesses compared to the corresponding TMD containing S. In all cases, the energy shift decreases as the number of layers increases,

following an inverse square dependence. This thickness dependence seems to disappear for more than 3-4 layers. The inverse square dependence of the energy shift on thickness can be attributed to quantum confinement effects that become more pronounced as the thickness decreases [28, 29]. Therefore, for materials that are 1-3 layers thick, we need to distinguish the energy shift of the plasmon peak due to changes in temperature from effects due to different sample thickness. This is achieved by measuring the temperature dependence of the plasmon energy shift separately for various 2D material thicknesses and applying the appropriate calibration measurement to map the temperature in area of known thickness.

Using the thickness dependent plasmon energy shifts, we determined the temperature distribution with nanometer-scale resolution in a $MoSe_2$ nanoflake, shown in the high-angle annular dark field (HAADF) image in Figure 2A, and correlated plasmon-energy shift with the corresponding temperature map (shown in Figure 2B). This temperature map was created using the low-loss EELS signals acquired over the entire $MoSe_2$ flake, consisting of areas with different sample thickness labelled as I, II, III that are 1, 2, and 3 layers thick, respectively. Using the calibrations shown in Figures 1D-F to account for the variation in thickness, a temperature map was produced for a $MoSe_2$ nanoflake at a setpoint temperature of 573 K. The overlay of the HAADF image and the temperature map (Figure 2C) shows that, for the regions (I, II, III), we measured a temperature of approximately 586K using the plasmon energy shift. Histograms showing the variation in temperature measured in each area are shown in Figure 2D. The temperature distributions are almost Gaussian and by fitting a Gaussian function to the distribution, a mean temperature was calculated for each region. The error is expressed as the percentage difference from the holder temperature set point (573 K). The measurements for area (I, II, III) are 592K (3.3%), 591K (3.1%), and 576K (0.5%), respectively. One source of error in our measurements is related to finding the center of the plasmon peak, accounting for an uncertainty of $\pm$22 meV, which is relatively small compared to peak shift of 270 meV per 100 K temperature difference in WSe_2, and corresponds to a temperature uncertainty of 8 K. For mapping the edges of the 2D layers, there is an additional source of error due to changes in the plasmon peak shape at the layer edges [33]. This effect is visible in the temperature map, where the edges of the 2D layers appear cooler than the rest of the layer. However,the overall consistency and accuracy demonstrated in the measured temperature is well within the error of the sample holder temperature setpoint, demonstrating that our technique is capable of mapping the

temperature distribution at the nanoscale in 2D materials.

Thus far, our temperature measurements have been presented empirically, using a calibration curve of the plasmon energy shift as a function of temperature (dE/dT). Next, we will show that the rate of this change is related to the lattice strain and the thermal expansion coefficient (TEC) of the material. This relationship is thickness-dependent due to the quantum confinement effects and underpins our temperature measurements. Within the free electron model, the plasmon energy is expressed as

$$E(T) = \hbar\sqrt{\frac{n(T)e^2}{\varepsilon_0 m}}, \tag{1}$$

where m and e are the mass and charge of an electron. The temperature dependence of the electron density $n(T)$ is due to the temperature dependence of volume $V(T)$ of the valence electron cloud $n(T) = \frac{n_0}{V(T)}$, where n_0 is the number of valence electrons). Hence, dE/dT (measured experimentally) can be expressed in terms of the change in the plasmon energy as a function of the lattice parameters (determined computationally as discussed below) and the TEC. A more general derivation of dE/dT in terms of strain-induced plasmon shifts and TECs is provided in the Supplementary Material. We will employ this effect to determine the TECs for all five free-standing 2D materials studied here.

To determine the plasmon loss curves and the subsequent energy shifts as a function of the changes in the lattice parameters, we applied the random phase approximation (RPA) [34], a well-known approach for the calculation of frequency-dependent dielectric function ($\varepsilon(\omega)$, which has been integrated into the Vienna Ab-Initio Simulation Package (VASP) (see Methods Section) [35]. In these calculations, the frequency dependent dielectric function is determined including local field effects, which allows calculation of the low-loss EEL spectra (which is proportional to $Im(-1/\varepsilon)$. Low-loss EELS of graphene and TMDs were calculated for 10 different in-plane lattice constants, $a/a_0 = 0.97 - 1.04$, which correspond to the in-plane lattice parameters at different sample temperatures. For bulk materials, we also performed calculations with different out-of-plane (c) lattice parameters, and their corresponding plasmon energy shifts were determined by extrapolating the measured energy shifts shown in Figures 1C-E to the limit of infinitely large sample thickness.

An example of the calculated low-loss EEL spectra for graphene is shown in Figure 3A. We found a linear relationship between the plasmon energy and the lattice constant, shown

in Figure 3B. With this computed relationship and the experimentally measured plasmon energy shift, the in-plane TECs were obtained for both thin films and bulk materials. The results are shown graphically in Figure 3C. Table I provides a complete list of TECs derived from our measurements and calculations for single-, double-, tri-layer as well as bulk materials. The error-bars in Table I are computed using the scatter in the experimental data shown in Figures 1C-E. Our predicted TEC values are compared with values available in the literature [36–44]. More details of the methods used to compute TECs are provided in the Supplementary Material.

As can be seen from Table I, our predictions for bulk materials are a close match with previously reported experimental data, especially for graphite, $MoSe_2$ and WSe_2. The consistency between the data reported here and the previously published data for bulk materials shows that the temperature dependence of the plasmon energy can be directly correlated to the thermal expansion. One important result of this study is that we experimentally measured the in-plane TECs for free-standing monolayer, bilayer and trilayer TMDs. For monolayer TMDs, we found that the in-plane TECs agree well with the theoretical results [36] showing increased TEC values up even more than one order of magnitude compared to their bulk structures. This is consistent with our other observation that as the thickness increases from 1 layer to 3 layers (for graphene and TMDs), the TEC decreases.

While our reported TECs for TMDs agree very well with published values, the calculated TEC value for graphene differs substantially from the reference data while still exhibiting the correct overall trend. This likely arises from the very high thermal and electrical conductivity in graphene compared to the semiconducting TMDs. In particular, the temperature in nanoflakes of graphene is correlated to the mean free path of phonons, which is orders of magnitude larger in graphene compared to TMD materials. This means that the thermal transfer between the graphene and the carbon support is much more efficient than for the TMDs, and the temperature measurement is much less local. Another factor that may influence the difference between our measurements and the reference is substrate clamping. As the reference data are measured for graphene grown on a substrate, the TEC for free-standing graphene should be significantly larger.

To further demonstrate our ability to map the thermal expansion coefficient of free-standing 2D materials, we acquire maps of the plasmon peak in $MoSe_2$ nano-flakes at 473 K and 623 K (see Video 1 in the Supplementary Material). The relative plasmon-peak shift as

a function of position is measured and used to determine the TEC using the first-principles modeling results described above. Figure 4A shows a free-standing $MoSe_2$ flake at 623 K, as well as the measured thermal expansion coefficient. The region of the $MoSe_2$ shown in Figure 4A consists two different layers, each exhibiting a different thermal expansion coefficient ranging between 0.25 and 1.06×10^{-4} K^{-1}. It is interesting to note here that the double layer area appears to exhibit the highest thermal expansion coefficient, and a sharp decrease at the edges of the layer. Figure 4B shows a line profile of the edge between the double and 4-layer regions in $MoSe_2$. It appears that the spatial resolution of the thermal expansion coefficient map is 2.95 nm, and is mostly limited by the pixel size of the spectrum image. To get a sub-pixel estimate of the position of the edge, a complementary error function is fitted through the experimental data, revealing that the measured width of the interface can be as small as 2.1 nm, if smaller pixel sizes are used for mapping the plasmon peak shift.

Figure 4C shows an atomic-resolution HAADF image of a free-standing MoS_2 flake at elevated temperature (573 K) consisting of 4 distinctive layers and demonstrates that the spatial resolution for imaging (even at elevated temperatures) is better than 1 Å (Figure 4D). However, the spatial resolution limit for our TEC measurements at interfaces and defects using STEM-EELS is lower than this value, as the temperature measurements fundamentally depend on the mean free path of phonons and electrons [31]. More specifically, the localization of the EELS signal for a plasmon peak at 20 eV can be determined using the equation introduced by Egerton [45]:

$$d_{50} \approx \sqrt{\left(\frac{\lambda}{2\theta_E^{3/4}}\right)^2 + \left(\frac{0.6\lambda}{\beta}\right)^2} \approx 1.9nm, \tag{2}$$

where $\lambda = 2.51$ pm is the electron wavelength at 200 kV, $\theta_E = 0.06$ mrad is the characteristic scattering angle, and $\beta = 60$ mrad is the EELS collection angle. On the practical side, the current measurement resolution is also limited by spatial drift and the sensitivity of the 2D materials to extended electron beam exposure. Nevertheless, the spatial resolution shown in Figure 4B, is very close to the predicted theoretical limit at the given plasmon peak energy, and orders of magnitude better compared to the spatial resolution of 100 nm for optical techniques. Such a high resolution for TEC measurements is crucial for examining thermal expansion mismatch and strain in the latest sub-10 nm transistors [46], where

a direct measurements are only possible using our STEM-EELS method. Further improvements to the temperature resolution and accuracy can be achieved by increasing the energy resolution of the low-loss EEL spectra using, for example, a monochromated STEM instrument [39]. More importantly, the measurement rate of our technique is very high, providing the capability of capturing dynamic temperature changes. The exposure time for low-loss EELS can be as low as 10^{-3}s,with a sufficient signal/noise ratio for most thin materials. This provides a great potential for in-situ thermal experiments involving dynamic processes. Finally, it should be noted that a potential issue arises from electron beam-induced sample heating effects. However, using a thermal conductivity, κ, of around 1 $Wm^{-1}K^{-1}$ for WSe_2 [47], we found a beam-induced temperature rise of only $\Delta T \approx 0.95$ mK for the electron probe conditions used. This value is significantly smaller than the temperature resolution of our EELS based measurement, and may safely be neglected. Details of the beam heating contributions are discussed in the Supplementary Material.

In summary, we have presented a novel approach to nanoscale mapping of TECs in freestanding 2D materials using high-resolution STEM imaging coupled with EEL spectroscopy. The measurement utilizes the shift in the plasmon peak of the 2D material, which is related to the thermal expansion of the 2D lattice. The measured plasmon energy shift exhibits a dependence on the number of 2D layers, which is attributed to quantum confinement effects in 2D materials. Accounting for the sample thickness of the 2D material, in units of number of atomic layers, we showed that it is possible to map the local temperature with nanometer resolution. Theoretical calculations using DFT and RPA were also developed to compare the thermal expansion coefficients of 2D and bulk materials, and the results are found to be in quite good agreement with existing reference data. By measurement of the TEC near surfaces, grain boundaries or heterointerfaces, we can predict and control the mismatch and thermal strain resulting from various device operations, avoiding strain induced (thermomechanical) fracture or changes in the electronic properties. This is particularly important for 2D materials, where temperature changes can cause strains on both sides of the interface due to the thickness dependence of the TEC. Future studies examining temperature variations across hetero-interface or grain boundaries, or other low-dimensional structures such as nanowires, in-plane heterostructures, and hybrid nanostructures will be essential to further elucidate our understanding of the thermal transport properties in nano-scale devices.

ACKNOWLEDGMENTS

X. H., A. S. K. and R. F. K. were supported by the National Science Foundation EFRI 2-DARE Grant 1542864. Dr. D. P. Bailey of the University of Illinois College of Engineering assisted in the copy-editing of the manuscript. The acquisition of UIC JEOL JEM ARM200CF is supported by an MRI-R^2 grant from the National Science Foundation (Grant No. DMR-0959470). This work made use of instruments in the Electron Microscopy Service and the High Performance Computing Clusters at Research Resources Center, UIC. This work used resources of the National Energy Research Scientific Computing Center, a DOE Office of Science User Facility supported by the Office of Science of the U. S. Department of Energy under Contract No. DE-AC02-05CH11231.

---

[1] A. K. Geim and K. S. Novoselov, Nature Materials **6**, 183 (2007).

[2] K. I. Bolotin, K. J. Sikes, Z. Jiang, M. Klima, G. Fudenberg, J. Hone, P. Kim, and H. L. Stormer, Solid State Communications **146**, 351 (2008).

[3] A. A. Balandin, S. Ghosh, W. Bao, I. Calizo, D. Teweldebrhan, F. Miao, and C. N. Lau, Nano Letters **8**, 902 (2008).

[4] F. Schwierz, Nature Nanotechnology **5**, 487 (2010).

[5] Z. Yan, G. Liu, J. M. Khan, and A. A. Balandin, Nature Communications **3** (2012).

[6] W. Han, R. K. Kawakami, M. Gmitra, and J. Fabian, Nature Nanotechnology **9**, 794 (2014).

[7] B. Radisavljevic, A. Radenovic, J. Brivio, V. Giacometti, and A. Kis, Nature Nanotechnology **6**, 147 (2011).

[8] W. J. Yu, Q. A. Vu, H. Oh, H. G. Nam, H. Zhou, S. Cha, J.-Y. Kim, A. Carvalho, M. Jeong, H. Choi, A. H. Castro Neto, Y. H. Lee, and X. Duan, Nature Communications **7** (2016).

[9] F. H. L. Koppens, T. Mueller, P. Avouris, A. C. Ferrari, M. S. Vitiello, and M. Polini, Nature Nanotechnology **9**, 780 (2014).

[10] Y. Li, W. Zhou, H. Wang, L. Xie, Y. Liang, F. Wei, J.-C. Idrobo, S. J. Pennycook, and H. Dai, Nature Nanotechnology **7**, 394 (2012).

[11] R. Murali, K. Brenner, Y. Yang, T. Beck, and J. D. Meindl, IEEE Electron Device Letters **30**, 611 (2009).

[12] L. Britnell, R. V. Gorbachev, R. Jalil, B. D. Belle, F. Schedin, A. Mishchenko, T. Georgiou, M. I. Katsnelson, L. Eaves, S. V. Morozov, N. M. R. Peres, J. Leist, A. K. Geim, K. S. Novoselov, and L. A. Ponomarenko, Science **335**, 947 (2012).

[13] Q. H. Wang, K. Kalantar-Zadeh, A. Kis, J. N. Coleman, and M. S. Strano, Nature Nanotechnology **7**, 699 (2012).

[14] D. Lembke, S. Bertolazzi, and A. Kis, Accounts Of Chemical Research **48**, 100 (2015).

[15] P. Yasaei, A. Fathizadeh, R. Hantehzadeh, A. K. Majee, A. El-Ghandour, D. Estrada, C. Foster, Z. Aksamija, F. Khalili-Araghi, and A. Salehi-Khojin, Nano Letters **15**, 4532 (2015).

[16] A. Majumdar, J. Lai, M. Chandrachood, O. Nakabeppu, Y. Wu, and Z. Shi, Review Of Scientific Instruments **66**, 3584 (1995).

[17] Y. De Wilde, F. Formanek, R. Carminati, B. Gralak, P.-A. Lemoine, K. Joulain, J.-P. Mulet, Y. Chen, and J.-J. Greffet, Nature **444**, 740 (2006).

[18] A. Soudi, R. D. Dawson, and Y. Gu, ACS Nano **5**, 255 (2011).

[19] F. Menges, H. Riel, A. Stemmer, and B. Gotsmann, Nano Letters **12** (2012).

[20] F. Menges, P. Mensch, H. Schmid, H. Riel, A. Stemmer, and B. Gotsmann, Nature Communications **7** (2016).

[21] I. Calizo, A. A. Balandin, W. Bao, F. Miao, and C. N. Lau, Nano Letters **7**, 2645 (007).

[22] K. Okabe, N. Inada, C. Gota, Y. Harada, T. Funatsu, and S. Uchiyama, Nature Communications **3**, 705 (2012).

[23] C. D. S. Brites, P. P. Lima, N. J. O. Silva, A. Millan, V. S. Amaral, F. Palacio, and L. D. Carlos, Nanoscale **4**, 4799 (2012).

[24] H. Watanabe, Journal of the Physical Society of Japan **11**, 112 (1956).

[25] G. Meyer, Zeitschrift für Physik **148**, 61 (1957).

[26] H. Abe, M. Terauchi, and M. Tanaka, Journal Of Electron Microscopy **44**, 45 (1995).

[27] H. Abe, M. Terauchi, R. Kuzuo, and M. Tanaka, Journal Of Electron Microscopy **41**, 465 (1992).

[28] M. Mitome, Y. Yamazaki, H. Takagi, and T. Nakagiri, Journal Of Applied Physics **72**, 812 (1992).

[29] Y. Wang, J. Kim, G. Kim, and K. Kim, Applied Physics Letters **88**, 143106 (2006).

[30] T. Eberlein, U. Bangert, R. R. Nair, R. Jones, M. Gass, A. L. Bleloch, K. S. Novoselov, A. Geim, and P. R. Briddon, Physical Review B **77**, 233406 (2008).

[31] M. Mecklenburg, W. A. Hubbard, E. R. White, R. Dhall, S. B. Cronin, S. Aloni, and B. C. Regan, Science **347**, 629 (2015).

[32] See Supplemental Material [URL] for description of experimental methods and first principles modeling as well as additional data of the EELS plasmon peak shifts as a function of temperature, which includes Refs. [48–51].

[33] W. Zhou, S. J. Pennycook, and J.-C. Idrobo, Ultramicroscopy **119**, 51 (2012).

[34] S. Louie, J. Chelikowsky, and M. Cohen, Physical Review Letters **34**, 155 (1975).

[35] G. Kresse and J. Hafner, Physical Review B **47**, 558 (1993).

[36] D. J. Late, S. N. Shirodkar, U. V. Waghmare, V. P. Dravid, and C. N. R. Rao, ChemPhysChem **15**, 1592 (2014).

[37] Y. Ding and B. Xiao, RSC Advances **5**, 18391 (2015).

[38] R. Murray and B. Evans, Journal Of Applied Crystallography **12**, 312 (1979).

[39] S. Elmahalawy and B. Evans, Journal Of Applied Crystallography **9**, 403 (1976).

[40] L. H. Brixner, Journal of The Electrochemical Society **110**, 289 (1963).

[41] A. Matthaus, A. Ennaoui, S. Fiechter, S. Tiefenbacher, T. Kiesewetter, K. Diesner, I. Sieber, W. Jaegermann, T. Tsirlina, and R. Tenne, Journal Of The Electrochemical Society **144**, 1013 (1997).

[42] N. Mounet and N. Marzari, Physical Review B **71**, 205214 (2005).

[43] W. Pan, J. Xiao, J. Zhu, C. Yu, G. Zhang, Z. Ni, K. Watanabe, T. Taniguchi, Y. Shi, and X. Wang, Scientific Reports **2**, 893 (2012).

[44] A. Bailey and B. Yates, Journal Of Applied Physics **41**, 5088 (1970).

[45] R. F. Egerton, *Electron Energy Loss Spectroscopy in the Electron Microscope* (Plenum Press, New York, 1986).

[46] A. D. Franklin, M. Luisier, S.-J. Han, G. Tulevski, C. M. Breslin, L. Gignac, M. S. Lundstrom, and W. Haensch, Nano Letters **12**, 758 (2012).

[47] A. Mavrokefalos, N. T. Nguyen, M. T. Pettes, D. C. Johnson, and L. Shi, Applied Physics Letters **91**, 171912 (2007).

[48] M. Asadi, K. Kim, C. Liu, A. V. Addepalli, P. Abbasi, P. Yasaei, P. Phillips, A. Behranginia, J. M. Cerrato, R. Haasch, P. Zapol, B. Kumar, R. F. Klie, J. Abiade, L. A. Curtiss, and A. Salehi-Khojin, Science **353**, 467 (2016).

[49] Y. Hernandez, V. Nicolosi, M. Lotya, F. M. Blighe, Z. Sun, S. De, I. T. McGovern, B. Holland, M. Byrne, Y. K. Gun'ko, J. J. Boland, P. Niraj, G. Duesberg, S. Krishnamurthy, R. Goodhue, J. Hutchison, V. Scardaci, A. C. Ferrari, and J. N. Coleman, Nature Nanotechnology **3**, 563 (2008).

[50] A. Politano and G. Chiarello, Nanoscale **6**, 10927 (2014).

[51] E. R. White, M. Mecklenburg, B. Shevitski, S. B. Singer, and B. C. Regan, Langmuir **28**, 3695 (2012).

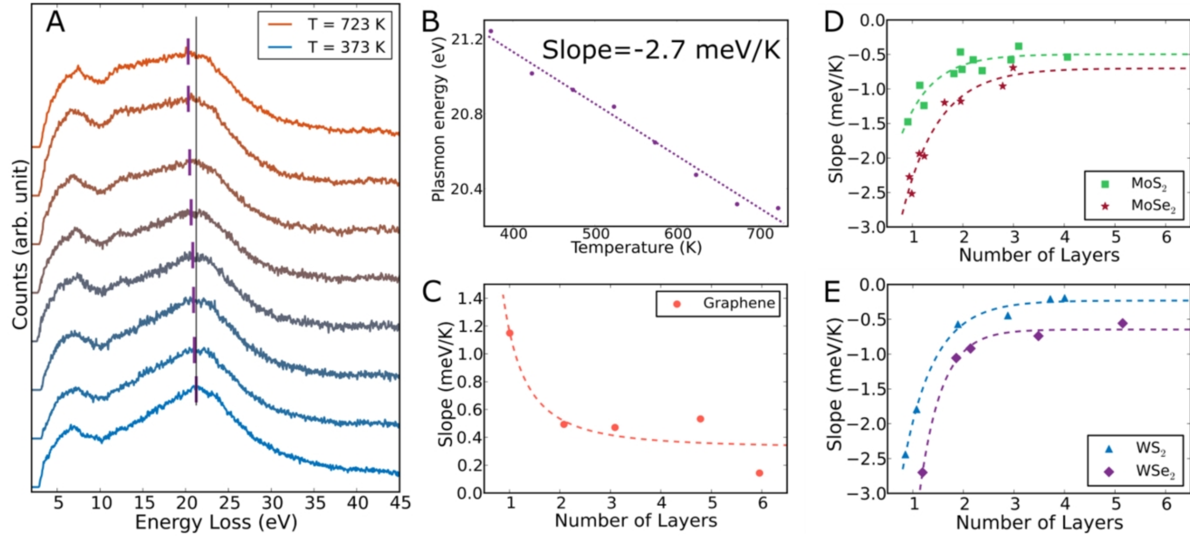

FIG. 1. (Color online) A) Low-loss EELS spectra from a monolayer of WSe_2 for temperatures between 373 K and 723 K. The purple lines indicate the plasmon peak centers for each temperature, determined by fitting two Lorentzian curves to the peak. The black line shows the plasmon peak center at a temperature of 373 K for comparison. B) The plasmon energy for each spectrum from (A) as a function of the temperature. C-E) The energy shifts (dE/dT) as a function of the number of layers of graphene, MoS_2, $MoSe_2$, WS_2, and WSe_2, respectively.

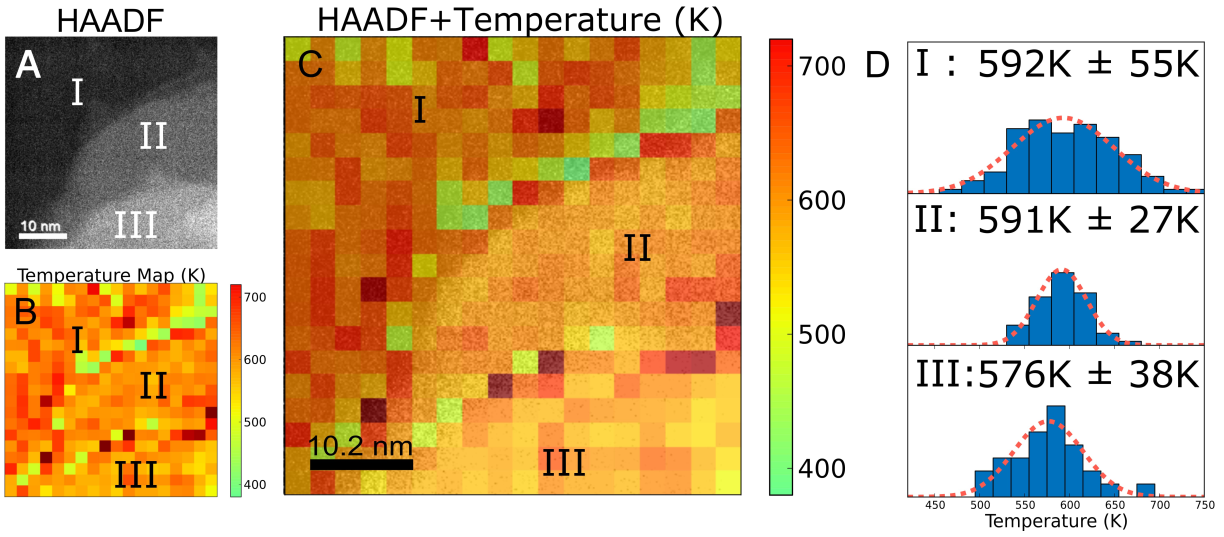

FIG. 2. (Color online) A) HAADF image of a $MoSe_2$ nanoflake. B) Corresponding temperature map of $MoSe_2$ at a nominal sample temperature of 573 K. C) The overlayed image of A) and B) showing three zones defined by the different thickness (I, II, III). D) The temperature distribution for each area.

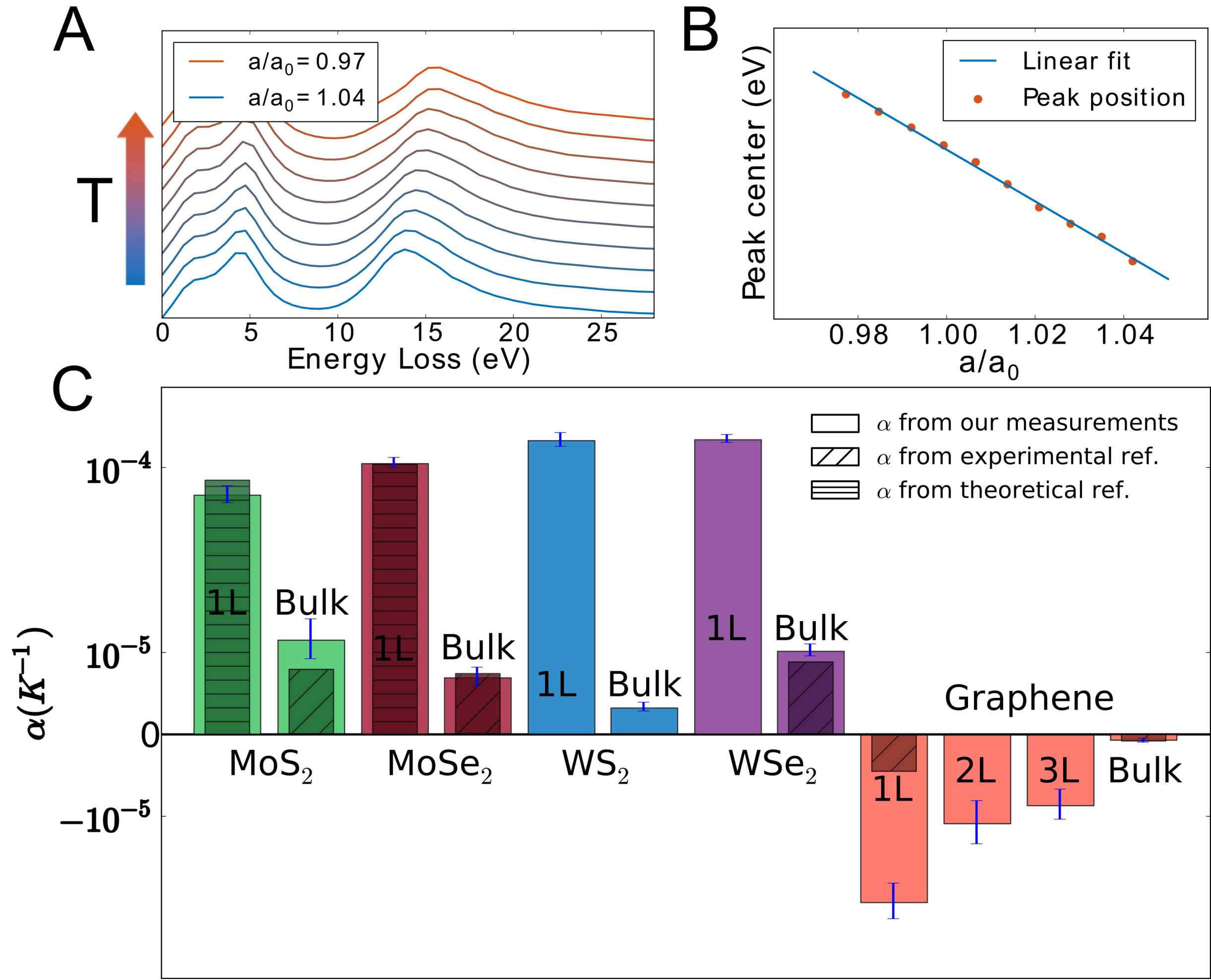

FIG. 3. (Color online) A) Calculated low-loss EEL spectra for single-layer graphene with different lattice constants. B) The plasmon energy for each spectrum from (A) as a function of lattice constant a. C) Measured in-plane TECs in thin films and bulk of graphene and TMDs, compared with reference data [36, 39, 43, 44]. The error bars are shown in blue and are calculated using the experimental uncertainty in determining the plasmon energy shift.

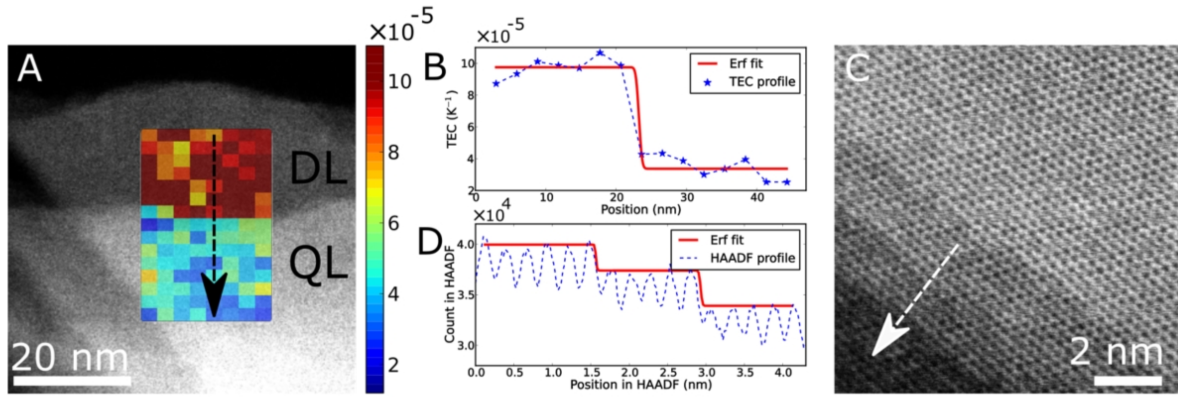

FIG. 4. (Color online) A) HAADF image of $MoSe_2$ at 623 K and the spatially resolved map of the local thermal expansion coefficient in the edge between double layer (DL) and 4-layer (QL) areas. B) Line profile of thermal expansion coefficient of the interface indicated by the black line in A. C) Representative atomic-resolution HAADF image of MoS_2 taken at 573 K. D) Line profile of image contrast across several layers of MoS_2 at 573 K.

System	Monolayer	Bilayer	Trilayer	Bulk
MoS_2	6.49±0.75 ($8.24^{a\dagger}$)	3.60±0.47	1.82±0.25	1.15±0.23 ($0.66^{b\dagger}$, $0.49^{c\ddagger}$-$0.79^{d\ddagger}$)
$MoSe_2$	10.62±0.64 ($10.54^{a\dagger}$)	5.44±0.35	3.46±0.28	0.69±0.10 ($0.64^{b\dagger}$, $0.74^{d\ddagger}$)
WS_2	15.21±1.38	2.26±0.20	1.31±0.10	0.32±0.04 ($-0.15^{b\dagger}$, $0.64^{f\ddagger}$)
WSe_2	15.42±0.69	4.18±0.25	2.74±0.29	1.01±0.06 ($0.55^{b\dagger}$, $0.68^{e\ddagger}$-$1.41^{f\ddagger}$)
Graphene	-2.14±0.37 ($-0.31^{g\dagger}$, $-0.45^{h\ddagger}$)	-1.09±0.25	-0.87±0.17	-0.07±0.01 ($-0.04^{g\dagger}$, $-0.08^{i\ddagger}$)

[a] Ref. 36, [b] Ref. 37, [c] Ref. 38, [d] Ref. 39. [e] Ref. 40, [f] Ref. 41, [g] Ref. 42, [h] Ref. 43, [i] Ref. 44.

TABLE I. Comparison of in-plane TECs (10^{-5} K^{-1}) obtained from our plasmon energy shift measurements and corresponding RPA calculations with reference (theoretical† and experimental‡) data [36–44].